

Accepted Manuscript

Petroleum Geoscience

Investigating controls on salt movement in extensional settings using finite element modelling

James Hamilton-Wright, Stephen Dee, Christina von Nicolai & Howard Johnson

DOI: <https://doi.org/10.1144/petgeo2018-119>

Received 30 August 2018

Revised 21 March 2019

Accepted 22 March 2019

© 2019 The Author(s). Published by The Geological Society of London for GSL and EAGE. All rights reserved. For permissions: <http://www.geolsoc.org.uk/permissions>. Publishing disclaimer: www.geolsoc.org.uk/pub_ethics

Supplementary material at <https://doi.org/10.6084/m9.figshare.c.4446272>

To cite this article, please follow the guidance at http://www.geolsoc.org.uk/onlinefirst#cit_journal

Manuscript version: Accepted Manuscript

This is a PDF of an unedited manuscript that has been accepted for publication. The manuscript will undergo copyediting, typesetting and correction before it is published in its final form. Please note that during the production process errors may be discovered which could affect the content, and all legal disclaimers that apply to the journal pertain.

Although reasonable efforts have been made to obtain all necessary permissions from third parties to include their copyrighted content within this article, their full citation and copyright line may not be present in this Accepted Manuscript version. Before using any content from this article, please refer to the Version of Record once published for full citation and copyright details, as permissions may be required.

Investigating controls on salt movement in extensional settings using finite element modelling

James Hamilton-Wright^{1*}, Stephen Dee¹, Christina von Nicolai¹ & Howard Johnson²

¹BP Exploration Operating Company Limited, Chertsey Road, Sunbury-on-Thames, Middlesex, TW16 7LN

²Department of Earth Science & Engineering, Imperial College London, Prince Consort Road, London, SW7 2BP

* Corresponding author (e-mail: james.hamilton-wright@bp.com)

Abstract: Salt structures present numerous challenges for targeting reservoirs. Salt movement within the subsurface can follow complex pathways, producing deformation patterns in surrounding strata which are often difficult to decipher. Consequently, the relative role of key salt flow drivers and geological sensitivities on salt structure evolution are often poorly understood. To address this, we have developed 2D geomechanical models using the finite element method to simulate salt diapir and pillow development in two extensional tectonic settings. We conducted model sensitivity analyses to examine the influence of geological parameters on field-scale salt structures and their corresponding deformation pattern. Modelled diapirs developing in thin-skinned extensional settings closely resemble published analogue experiments, however active and passive stages of diapir growth are seldom or never reached, respectively, thus challenging existing ideas that diapir evolution is dominated by passive growth. In all modelled cases, highly strained domains bound the diapir flanks where extensive small-scale faulting and fracturing can be expected. Asymmetric diapirs are prone to flank collapse and observed in models with fast extension or sedimentation rates, thin roof sections or salt layers, or initially short or triangular shaped diapirs. In modelled thick-skinned extensional settings, salt pillows and suprasalt overburden faults can be laterally offset (decoupled) from a reactivating basement fault. This decoupling increases with increased salt layer thickness, overburden thickness, sedimentation rate and fault angle, and decreased fault slip rates. Contrary to existing consensus, overburden grounding onto the basement fault scarp does not appear to halt development of salt structures above the footwall basement block.

Supplementary material: Animations for all model runs are available at <https://doi.org/10.6084/m9.figshare.c.4446272>.

Introduction

Most of the world's salt basins have been affected by salt tectonic activity throughout their evolution (Hudec & Jackson 2007). Constituting prolific hydrocarbon provinces, they have also been of major interest to the petroleum industry for many years. Once mobilised, salt flows to form characteristic shapes and structures (diapirs) whilst simultaneously deforming the surrounding strata via fracturing, faulting and bed rotation. This may cause the development of complex deformation patterns which are difficult to decipher but bear significant risks for hydrocarbon exploration and production. Key subsurface risks associated with salt include source rock maturity, reservoir presence and compartmentalisation, charge access, and trap failure. Drilling near or through salt structures is associated with additional risks as salt bodies alter the local stress field, impacting pore pressure and wellbore stability predictions. Understanding the evolution of salt structures and their associated fault and fracture pattern is of major importance across the value chain, from exploration and appraisal to field development and production.

Traditionally, salt structure evolution has been studied using analogue models, scaled three-dimensional sandbox models in which a viscous polymer and a sand or other granular material are used to represent salt and brittle overburden respectively (e.g. Ge & Vendeville 1997; Dooley *et al.* 2003, 2005). Many of the fundamental concepts of salt diapir growth have been derived from these models, and recent advances in digital photogrammetry even allow determination of particle displacement patterns and strain distribution. High resolution monitoring equipment is still only available in few laboratories and finding appropriate materials to represent the stratigraphy has remained challenging, particularly with regard of dynamic scaling requirements (Archer *et al.* 2012). Analogue models tend to overestimate buoyancy forces and are incapable of accounting for pressure gradients or variations in sediment strength over time (Allen & Beaumont 2012).

In recent years the use of computational models has become increasingly popular in salt tectonics research. Technology now enables generation of high-resolution geomechanical models incorporating realistic scaling and physically correct material properties to reconstruct structural development over geological timescales. Numerical modelling codes attempt to solve boundary problems for differential equations describing rock deformation. In Finite Element Modelling (FEM) approximate solutions are determined by breaking the model down into “finite elements”, which permits modelling of very complex geometries and capturing local effects such as stress and strain distribution near salt diapirs (Reddy 1993).

Existing numerical models have principally studied salt movement and deformation on a basin-wide scale (e.g. Gemmer *et al.* 2004, 2005; Ings *et al.* 2004; Gradmann *et al.* 2009; Albertz *et al.* 2010); smaller scale models often have complex model set-ups, for example Schultz-Ela & Jackson (1996) examine discontinuous salt and salt at multiple levels. The remaining smaller scale models do not consider geological parameter sensitivities (e.g. Luo *et al.* 2012). In this study we present the results of two FEM experiments designed to study the evolution of salt structures in two different extensional tectonic settings. These are field-scale models (5–10 km), which are uncommon and of interest for field development planning. The modelling results were compared to those of published analogue experiments; this allowed us to examine the concepts of diapir growth derived from these experiments. Additionally, we tested the influence of different modelling parameters on salt structure evolution and the corresponding deformation pattern. In the first experiment we modelled the evolution of a salt diapir in response to thin-skinned extension of the sedimentary overburden. This phenomenon is frequently observed in, but not limited to, the proximal domain of passive margins where post-break up thermal cooling and sedimentary loading generates basal and surface slopes and thus triggers gravitational collapse (e.g. Rowan *et al.* 2004). In some cases, overburden extension with associated salt diapirism can also occur in response to basement tectonics, that is, thick-skinned extension (e.g. Krantz 1989). Our second experiment implemented this scenario via reactivation of a pre-existing basement fault beneath a salt layer. Such scenarios are very common in rift basins like the North Sea (e.g. Hodgson *et al.* 1992) or the Early Palaeozoic sedimentary basins of the Arabian plate (e.g. Al-Barwani & McClay 2008).

The modelling results helped us to address the following key questions, which have also been used to de-risk exploration targets in terms of drilling hazards and reservoir deliverability:

- (a) To what extent do our models agree with concepts derived from existing analogue and numerical experiments?
- (b) What role do parameter sensitivities play on influencing diapir and overburden geometries under thin-skinned extension?
- (c) How do parameter sensitivities impact suprasalt structure development above a reactivating basement fault, and does overburden grounding play a key role in limiting salt supply?
- (d) Is this modelling approach applicable for predicting key drivers of salt flow, hydrocarbon trap geometries, and the distribution of faults and fractures?

Mechanics of salt

The predominant trigger of salt movement is differential loading, which can be caused by either gravity, tectonics, or thermal forces (e.g. Vendeville & Jackson 1992a; Ge *et al.* 1997; Hudec & Jackson 2007). Gravity-driven salt flow can be further sub-divided into gravity gliding and gravity spreading. Whilst gravity gliding refers to the rigid translation of a rock mass in response to creation of a slope, gravity spreading describes the collapse of a salt body under a load that is acting on it (e.g. Rowan *et al.* 2004). Once sufficiently loaded with sediment salt starts to spread from beneath the depocentre and moves towards areas with smaller loads. This movement might be updip or downdip depending on basal and surface slope angles. Similarly, when tectonic forces induce faulting within the overburden section, this produces a load deficit along the fault plane and salt will move towards this area where the load is smallest. Hence, when faulting

dismembers the overburden salt can rise upwards in the stratigraphic section and form diapirs or even extrusive sheets upon reaching the surface. However, if faulting also creates a relief in the base of salt, flow might occur laterally and thus limit vertical salt rise. Which of the two dominates will ultimately determine the types and distribution of salt structures within a basin and is dependent on the forces opposing salt flow, that is, the frictional forces at the interface between salt and over/underburden and the mechanical strength of the cover sediments. If the latter is too high for significant faulting to occur, then vertical salt rise and diapirism will not take place. Instead, salt may flow laterally accumulating elsewhere, or remain stationary with stresses being accommodated exclusively by the overburden.

The tendency of salt to follow elevation and load gradients is analogous to that of a liquid responding to hydraulic head gradients. Over geological times (i.e. low strain rates) salt is therefore considered to behave like a Newtonian fluid, and salt movements can be described using the laws of hydrodynamics. Comprehensive summaries of how these laws are translated to describe subsurface salt flow have been given by Hudec & Jackson (2007) and Gemmer *et al.* (2004, 2005). Salt flow typically occurs at much higher rates than most upper crustal deformation. For example, salt extrusion rates above Iranian diapir vents studied by Talbot *et al.* (2000) indicated extremely rapid extrusion rates up to 2-3 m/year. A further consequence of this fluid-like behaviour is that salt is relatively incompressible i.e. the effects of stress on salt density are negligible, and thus becomes buoyant once buried beneath denser rocks (Hudec & Jackson 2007). Hence, buoyancy is another mechanism for triggering salt flow; yet generally only becomes important during the more mature stages of diapir growth when a thick sedimentary cover has accumulated. In most cases initial salt flow is caused by the above-mentioned gravitational loading, tectonic activity, or a combination of both. The interaction between the different drivers is complex and so are the resulting structures and the numerical codes required to model them accurately.

Methodology

Two numerical experiments were designed using the 2D plane-strain finite element software Elfen® developed by Rockfield Global, the details of which are discussed elsewhere (e.g. Thornton & Crook 2014). These are similar to generic feature models: templates within which geometry, material properties, and physical properties can be altered efficiently to evaluate the solution space. This technique is therefore ideal for running sensitivity analyses, whereby selected geological parameters are varied against a reference model (Table 1) to assess their impact on (i) salt structure and overburden geometry, (ii) salt flow patterns, and (iii) the distribution of stress and strain. Simple models are designed to enable clear interpretation of sensitivities and are of hydrocarbon field-scale (5-10 km). Both models include a geostatic initialisation stage for applying initial vertical and lateral stresses in the domain i.e. loading of pre-kinematic overburden under gravity onto a viscous salt layer. Adaptive remeshing of the finite element grid allows treatment of large deformation and strains often associated with salt movement.

In both experiments overburden and syn-kinematic sediments are modelled as poro-elastoplastic (Table 2). A standard Mohr-Coulomb constitutive model is often utilised in numerical models, which is a generalisation of the Coulomb friction failure law to describe yielding of rocks under stress. This linear description of the yield surface under compressive normal stress describes purely elastic behaviour prior to failure, however rocks can experience a significant proportion of non-recoverable plastic deformation. Instead we utilise a more sophisticated Soft Rock 3 (SR3) critical state constitutive model designed by Rockfield Global, the fundamental concepts of which are explained in detail in Crook *et al.* (2006) and Thigpen *et al.* (2019). This is a significantly modified version of the standard Mohr-Coulomb model which includes the effects of compressive failure. An evolving curved yield function is governed by the void ratio or plastic volumetric strain via a piecewise linear hardening/softening law, similar to a critical state material model (Crook *et al.* 2006). For simplicity we consider drained effective stress models: initial porosity and pore fluid pressure are defined, however changes in pore pressure are not considered in the model computation (Table 2). An initial

bulk density of 2400 kg/m^3 is used to represent a sand-dominated sequence (e.g. Allen & Allen 2013). Models include dynamic rescaling, and the initial mass scaling constant is set at 10^{-6} , which is utilised to increase the timestep where the results will not be affected by a change in mass (Rockfield Global 2015). Salt is modelled as a viscoplastic material using a Newtonian fluid model for simulating flow (Table 2), which is discussed in standard hydrodynamic texts. This model describes a simple linear relation between shear stress and strain rate, and fluid viscosity is constant. The initial mass scaling constant is such that salt viscosity has been scaled from 10^{19} Pa.s to 0.3 Pa.Ma . Basement, where incorporated, is modelled as an isotropic material with a very high Young's modulus to simulate rigid basement blocks (Table 2).

Experiment 1 simulates a diapir evolving under extension, as described in Figure 1(a). A pre-existing diapir overlies a mother salt layer, contained within a pre-kinematic sand-dominated overburden sequence. In addition, accumulation of syn-kinematic sediments is simulated via the aggregation method, whereby layers are deposited incrementally with a horizontal upper boundary until a specified horizon is reached. This horizon is set at 100 m above the previous sediment layer or initial model top boundary, and applied in eight stages at 1 Myr increments equivalent to an average sedimentation rate of 0.1 mm/yr. The model top boundary is unconstrained, whilst the left-hand vertical and basal model boundaries have fixities applied. Tectonic loading equivalent to 5000 m of horizontal extension is applied to the right-hand vertical boundary over the 8 Myr run time.

Experiment 2 simulates the response of a mother salt layer and pre-kinematic overburden to a reactivating basement fault under extension (Fig. 1b). Syn-kinematic sediments are simulated via the aggregation method: the layer horizon is set 50 m above the previous sediment layer or initial model top boundary, and applied in two stages at 1 Myr increments equivalent to an average sedimentation rate of 0.05 mm/yr. The model top boundary is unconstrained, whilst the left-hand vertical and basal model boundaries have fixities applied. Vertical tectonic loading is applied to the top basement boundary to the right-hand side of the basement step to simulate 500 m displacement along a basement normal fault over 2 Myr. The right-hand vertical boundary has tectonic loading applied which matches the horizontal slip component of the basement fault, so that space is not created within the model. Table 3 summarises the geological parameter ranges tested and their justifications.

Effective plastic strain ($\bar{\epsilon}_p$) is considered a failure indicator, which increases whenever the material is actively yielding i.e. whenever the state of stress is on the yield surface. The value of effective plastic strain is the integral of stepwise increments of plastic deformation for a period of time, t :

$$\bar{\epsilon}_p = \int \frac{\delta \epsilon_p}{\delta t} \quad (1)$$

$$\delta \epsilon_p = \sqrt{\frac{2}{3} (\delta p_{ij})^2} \quad (2)$$

where $\delta \epsilon_p$ is the effective plastic strain increment, and δp_{ij} is the plastic strain tensor (Rockfield Global 2015). Model result plots are contoured by effective plastic strain as they effectively locate highly-strained areas and highlight localised shear zones that correspond to faults in rocks (Schultz-Ela & Jackson 1996). In addition, we contour by Yielding in Shear Flag, a normalised function for the SR3 constitutive model which indicates areas of yielding by shear failure (value of 1).

Results

All model animations are available in Supplementary Data online. Scaling is such that 5 s in animation time represents 1 Myr geological time.

Experiment 1: Diapir evolution under extension

Reference model (D-REF)

During geostatic initialisation, the diapir roof arches upwards in response to overburden differential loading. At 480 kyr a right-hand dipping fault develops in the diapir roof (Fig. 2a-b), shortly followed by an antithetic fault which creates a salt-cored graben (Fig. 2c-d, 920 kyr). As new sediments are deposited over the diapir, the zone of plastic strain propagates upwards causing roof thinning via faulting, and salt reactively rises into the newly generated space. At 1.14 Ma (Fig. 2e-f) the pre-kinematic roof completely thins, and subtle roof uplift above its regional level records the transition to ‘active’ salt movement. By 1.64 Ma (Fig. 2g-h) the syn-kinematic roof section also completely thins, exposing salt at the surface. Subsequently, the diapir rapidly widens in response to further extension, whilst newly deposited roof sediments quickly thin via faulting until salt is re-exposed, typically within 400 ka. Often roof faults localize in two locations; one structure quickly develops into a mature, symmetrical graben, whilst the other is abandoned (Fig. 2i). A structural cycle develops: salt reactively rises into the graben core, followed by a short active phase once the roof is sufficiently thin. This phase is characterized by roof bulging and ‘flap’ formation until a new sediment cover reburies the salt. Faults tend to localize in the thinnest roof section, which can vary in location at this stage. Hence, the diapir flanks comprise low-angle and high-angle sections against surrounding overburden. Continued salt rise beneath the thinned roof, coupled with an increasing sediment load causes the diapir flanks to deflate, creating an overburden rim syncline. The overburden starts to ground (6.52 Ma), cutting off salt supply and constraining salt rise to a narrow diapir apex, which generates high strain in the adjacent wall and cover strata. The diapir is roughly symmetrical and triangular in profile, flanked by a rim syncline sequence that progressively tracks towards the narrowing diapir apex with time. The rotated overburden ‘flaps’ remain highly strained close to the flank salt-sediment contact (Fig. 2j).

Altering extension rate

For model *D-EX0.25*, which tests a reduced extension rate of 0.25 mm/yr compared to the reference model, the initial roof fault forms above the diapir centre, which develops into a salt-cored graben (1.1 Ma). The surface emergence of salt is significantly delayed (2.7 Ma) compared to the reference model (1.64 Ma). The diapir flanks do not deflate; instead, the diapir progressively widens and inflates with a convex upward geometry, progressively rotating syn-kinematic strata to steeper dips (up to 44°). In this case the overburden does not ground through the mother salt layer to the model base. Roof graben structures develop in the syn-kinematic roof above the diapir centre. Accordingly, the final diapir is very symmetrical in profile (Fig. 3a). Diapir development in model *D-EX0.95*, which tests an increased extension rate of 0.95 mm/yr, is broadly similar compared to the reference model. However, roof faults proximal to the left side of the diapir preferentially uptake strain and develop into graben structures. Faults develop above the narrowing diapir apex at later stages. The overburden grounds relatively early (5.2 Ma). Consequently, salt rise is limited and extensive deflation of the diapir flanks creates a broader, shorter, slightly asymmetric diapir profile fringed by a thick rim syncline overburden sequence (Fig. 3b).

Altering diapir shape

In model *D-CURV*, designed with an initial curved diapir shape, the diapir develops symmetrically, forming a narrow apex and a thick rim syncline overburden sequence in response to flank deflation. The overburden grounds over a wide zone, and the overburden strata experience high strain at considerable distances (up to 4.1 km) from the diapir. In model *D-TRI*, designed with an initial triangular diapir shape, the diapir develops with a narrow apex, but salt rise is severely inhibited as the flanks here are prone to extensive sediment loading and deflate early. Consequently, the diapir has started to collapse, ponding sediments in an early minibasin sequence above the apex (Fig. 3c). For model *D-ROLL*, designed with an initial long-wavelength salt pillow,

faulting localizes above the left-side of the pillow crest. Salt rapidly exposes near the surface, followed by development of multiple faults in the roof overburden during phases of reburial. Preferential strain uptake on the right-hand structure progressively shifts the locus of salt rise to the right, creating a curved diapir profile (Fig. 3d).

Altering sedimentation rate

In model *D-SED0*, which does not include syn-kinematic sedimentation, the pre-kinematic roof rapidly thins to expose salt at surface (1.26 Ma). Under continued extension the salt body progressively widens, sourcing salt from the depleting mother salt layer. This salt supply is insufficient to cause viscous outflow i.e. salt glaciers at surface (Fig. 3e). Diapir development in model *D-SED0.05*, which tests an increased sedimentation rate of 0.05 mm/yr, broadly matches the reference model. However, sediments close to the diapir flank tend to experience higher strain (Fig. 3f). A thinner overburden rim syncline sequence reflects limited diapir flank deflation, insufficient for overburden grounding through the mother salt layer, and producing a convex upward diapir profile. Model *D-SED0.15*, which tests an increased sedimentation rate of 0.15 mm/yr compared to the reference model, develops a highly asymmetrical diapir profile. Faults localize within the syn-kinematic roof proximal to the right-hand flank (5 Ma), creating a wide, low-angle salt-sediment contact which preferentially ponds sediments (Fig. 3g). Reactive-active transitions are clearly preserved by uplifted roof ‘flaps’, highlighting periods of accelerated salt rise through thinned overburden.

Altering salt layer thickness

Model *D-S500* has a limited salt supply (500 m thick salt layer) relative to the reference model. Thus, the diapir flanks are prone to collapse by extensive sediment loading, causing the overburden sequence to ground. Initial roof faults localize proximal to the right-hand diapir flank, but faults in syn-kinematic strata develop above the diapir crest (Fig. 3h). In model *D-S1000*, which tests a thicker salt layer (1000 m) compared to the reference model, the initial roof faults localize above the diapir centre, and form sequentially above the narrowing diapir apex. However, where two graben structures develop simultaneously the right-hand structure generally accrues more slip and becomes the locus of salt rise, whilst the other is abandoned. The diapir inflates until 5 Ma with a convex-upward geometry. At this point sediment loading deflates the flanks and rotates the syn-kinematic strata back towards horizontal, causing high strain to affect areas out to considerable distances (up to 4 km) (Fig. 3i).

Altering diapir width

Roof faults only localise above the diapir crest in model *D-W1000*, which tests a reduced diapir width (1000 m) compared to the reference model, and therefore the diapir develops a symmetrical profile. The zone of high strain radiating from the diapir flanks varies considerably between layers (350–4900 m), and overburden folding is limited. In model *D-W3000*, which tests an increased diapir width (3000 m), roof faults preferentially localize proximal to the left-hand diapir flank. Therefore, the final profile is an approximate mirror image of the reference model, where roof faults initially localize proximal to the right-hand diapir flank. Deflation of the right-hand flank is more pronounced, creating a thicker rim overburden syncline. Final diapir width is *c.* 880 m wider than the reference model, similar to the initial width increase (1000 m).

Altering diapir height

During geostatic initialisation in model *D-H800*, designed with an increased diapir height (800 m) compared to the reference model, a greater structural relief develops in the diapir roof section in response to a thicker sediment load off structure. Structural development broadly matches the reference model. However, early salt breakthrough near the right-hand diapir flank is followed by extensive sediment loading of the left-hand flank

(from 4.5 Ma), creating a highly asymmetric profile (Fig. 3j). Model *D-H1200*, which tests a further increased diapir height (1200 m) compared to the reference model, also shows a pronounced structural relief during geostatic initialisation. In this case, salt breakthrough above the diapir centre causes a markedly different structural evolution. Faults localize above the central crest for the entire duration, and rapid flank deflation is observed as early as 3.2 Ma, developing a thick overburden rim syncline with steep dips (Fig. 3k). Roof arching and ‘flap’ rotation characterize multiple reactive-active transitions. Final diapir geometry is relatively narrow and symmetrical with steeper flanks, and syn-kinematic surrounding the diapir apex experience relatively very high strain.

Altering roof thickness

In model *D-R300*, designed with an increased roof thickness (300 m) compared to the reference model, the first graben structure is significantly broader (500 m compared to 270 m) and develops above the diapir centre. However, final structural geometry is similar (Fig. 3l). In model *D-R500*, designed with an increased roof thickness (500 m), the first graben structure to develop is many times broader (800 m) compared to the reference model and locates above the diapir centre. Up to 4 Ma the diapir widens and inflates, rotating strata away from the diapir. Later-stage sediment loading on the diapir flanks back-rotates the strata towards the diapir, and this process appears to strain the overburden to considerable distances (up to 4500 m). Final diapir geometry is complex, with well-defined high-angle and low-angle salt-sediment contacts (Fig. 3m).

Experiment 2: Reactivation of a basement step

Reference model (T-REF)

As a basement extensional fault reactivates and accumulates slip, the overlying salt deforms viscously by flowing into newly created space. Salt movement causes the suprasalt overburden to stretch and thin, and eventually accommodates deformation via faulting (120 kyr). A wide zone of small-displacement faults develops with a graben geometry. However, the left-hand border fault rapidly develops as a master fault, accommodating much of the strain (200 kyr) (Fig. 4a). The fault hanging-wall overburden starts to slip, and flexes into a long wavelength syncline as salt evacuates beneath the load. The other overburden faults cease activity, and a salt pillow develops within the master fault footwall (Fig. 4b). Salt progressively feeds pillow growth, causing the master fault to rotate to a shallower dip. At this point antithetic faults reactivate and/or develop, and hanging-wall overburden subsidence accelerates (Fig. 4c). The antithetic faults continue to slip, broadening the salt pillow and converting the fault array into an ‘hourglass’ structure (1.25 Ma) (Fig. 4d). The hanging-wall overburden continues to slip against the master fault until the antithetic fault here terminates into the crest of the salt pillow (1.7 Ma), converting the ‘hourglass’ structure into a salt-cored graben (Fig. 4e). Overburden flexure and subsidence continues until the overburden ‘grounds’ onto the basement step. The overburden becomes highly strained above the zone of complete salt evacuation (2.0 Ma) (Fig. 4f).

Altering fault slip rate

Model *T-F0.5* is designed with an increased fault slip rate of 0.5 mm/yr. Overburden faults develop rapidly (60 kyr) and constrained to a narrower zone compared to the reference model. The left-hand fault is abandoned, and a master fault rapidly develops (110 kyr) from a fault synthetic to the basement fault, which is closer to the basement step than its equivalent in the reference model. At 150 kyr an antithetic fault localizes within the main fault footwall, which progressively accrues slip to define the left-hand side of a horst structure (460 kyr) above an asymmetrical, reactive salt pillow (Fig. 4g). In model *T-F1.0*, designed with an increased fault slip rate of 1.0 mm/yr, the synthetic master fault (40 kyr) and subsequent horst structure (240 kyr) develop earlier than the reference model and *T-F0.5*, and locate closer to the basement step. Model *T-F2.5* tests a further increased fault slip rate of 2.5 mm/yr. A shear zone localises as early as 20 kyr and develops into a synthetic master fault (40 kyr). As with models *T-F0.5* and *T-F1.0*, a horst structure (120 kyr)

develops following antithetic fault development, and significantly earlier than the reference model. In addition, another synthetic fault initiates to the left of the horst (120 kyr), which later borders a graben (180 kyr) (Fig. 4h).

Altering sedimentation rate

In model *T-SED0*, designed with no syn-kinematic sedimentation, structural development is analogous to model *T-F1.0*. A synthetic master fault localizes close to the basement step, which bounds the right-hand edge of a subsequently developed horst structure (600 kyr). The left-hand, antithetic fault then overtakes as a master fault, and reactive salt rise accelerates into a high relief salt pillow below (1.6 Ma) (Fig. 4i). For model *T-SED0.2*, designed with an increased sedimentation rate (0.2 mm/yr) compared to the reference model, overburden faulting localizes significantly offset from the basement step, and strain uptake remains fairly distributed across several faults. By 580 kyr the outermost faults develop into master faults, defining an hourglass structure. This progressively widens, and a slight dominance of the synthetic fault converts the hourglass into a broad, salt-cored graben (1.56 Ma) (Fig. 4j).

Altering salt layer thickness

In model *T-S100*, designed with a reduced salt layer thickness (100 m) compared to the reference model, a synthetic overburden master fault rapidly develops (100 kyr) close to the basement step, with minor activity on other faults. From 500 kyr the zone of high strain broadens as the overburden grounds onto the basement step (1.24 Ma). This fault is then abandoned and replaced by two new synthetic faults: one in the footwall, and one as an overburden extension of the basement fault (Fig. 4k). In model *T-S400*, designed with an increased salt layer thickness (400 m) compared to the reference model, fault development is widely offset from the basement step. An antithetic master fault develops (150 kyr), followed by a synthetic fault creating a symmetrical graben (840 kyr), but late-stage dominance of the synthetic fault creates an asymmetric graben profile (Fig. 4l).

Altering overburden thickness

For model *T-O200*, which tests a decreased overburden thickness (200 m), an initial antithetic fault localizes (120 kyr) with a smaller offset from the basement step than the reference model. A synthetic fault then develops (300 kyr), and together they border a very narrow graben (360 m). The graben core is highly strained, with significant layer thinning and subtle arching indicating active salt rise (1.84 Ma) (Fig. 4m). In model *T-O1000*, which tests an increased overburden thickness (1000 m), a series of overburden faults localise with significant offset from the basement step, which are distributed over a wider area (1200 m) than the reference model. The synthetic faults activate diachronously: faults proximal to the basement step activate first, and from 400 kyr these accommodate much of the strain. These terminate into an antithetic fault, which develops into a master fault (1 Ma) upon continued overburden flexure. At 1.5 Ma a synthetic fault to the left-hand side of existing faults accrues strain until strain uptake broadly matches the antithetic fault, defining a wide, salt-cored graben (1700 m) (1.7 Ma). At this point internal faults are abandoned (Fig. 4n).

Altering basement fault angle

In model *T-FA50*, designed with a reduced basement fault angle (50°) compared to the reference model, a narrower zone of faulting develops in the overburden, but strain uptake similarly focuses onto a synthetic master fault. Graben development is consistent, although roof strata above the core experience higher strain (Fig. 4o). In model *T-FA70*, however, designed with an increased basement fault angle (70°), the graben develops slightly more offset from the basement step than the reference model (c. 400 m difference) (Fig. 4p). Rather than evolving from an hourglass structure as with the reference model, the graben develops directly

from an antithetic fault accompanying an established synthetic master fault, which terminate into a short, very broad salt pillow. This antithetic fault develops close to the basement step in response to rapid overburden flexure.

Discussion

Experiment 1: Diapir evolution under extension

In our first experiment a pre-existing narrow salt structure (diapir) was subject to thin-skinned extension. This diapir was elevated above an otherwise even mother salt layer with constant thickness. The base of the salt was fixed to model extension without basement involvement. In the different model runs parameters including the overburden extension rate, initial salt diapir geometry, mother salt thickness, and sedimentation rate were modified systematically to investigate the influence of these parameters on the resulting diapir geometry and deformation pattern.

The experiment set-up and procedure closely resemble the physical models of Vendeville & Jackson (1992a) who were the first to systematically study the rise of diapirs under thin-skinned extension. From their experiments the authors derived three stages of diapirism. The first stage, termed reactive, is characterised by rise of salt due to extension of the overburden. This extension causes thinning and fracturing of the sedimentary cover and the development of half graben and graben structures bounded by normal faults. Salt rises upwards along the graben axes to balance the established load gradient, forming triangular diapirs bounded by the graben faults. If continuous extension sufficiently weakened the overburden the diapir eventually reached a second, active stage, where salt movement is no longer dependent on extension but is driven by buoyancy forces within the salt. During active rise salt pushes aside the sedimentary cover, causing rotation of strata and fault blocks that formed in the preceding stage. This “flap rotation” can steepen strata adjacent to the diapir flanks and are distinct from the gentle strata dips of the reactive phase. Rapid vertical salt flow caused further diapir narrowing upwards, resulting in a plug-like shape. If the salt managed to fully pierce the overburden and emerge at the surface the diapir reached the third, passive stage. During passive growth, which is also known as downbuilding, sediments accumulate around the diapir with little roof sequence deposited. Depending on the rate of sedimentation versus salt rise the shape of passive diapirs varies from widening upwards (mushroom shape), constant widths (plug shape), or narrowing upwards. Accordingly, the geometries of the surrounding strata may vary from overturned beds to gentle onlapping of strata on the diapir’s flanks. Although extensional forces may contribute to passive diapirism the dominant mechanism is differential sedimentary loading induced by loading of the diapir flanks and reduced deposition over the diapir crest. It is thought that most of the world’s large salt domes and walls spent the largest part of their evolution as passive diapirs (Hudec & Jackson 2007). In fact, most early and some recent models (e.g. Trusheim 1960; Warsitzka *et al.* 2013) suggest that a diapir can initiate in passive stage, hence never evolving through the reactive and active stage. However, this requires very specific initial depositional conditions that in most sedimentary basins are probably not met. It is therefore widely accepted that the primary trigger for diapiric growth is extension, causing initial salt rise to be reactive in nature (Hudec & Jackson 2007).

In our models the reactive diapir stage is very well reproduced, with normal faults and graben structures forming within the thinned sedimentary cover and salt rising into the created space, creating a triangular shaped diapir (Fig. 2a-d). As the diapir widens and the mother salt layer depletes the older overburden sequences are pushed aside and subside. Thus, highly strained domains bound the diapir flanks while new faults continue to form above the diapir crest in the newly deposited layers (e.g. Fig. 2j). As in the experimental models of Vendeville & Jackson (1992a) the faults in the older layers become inactive once a new set form. Hence, older faults do not connect into younger strata and active faulting is confined to the diapir crest. An important observation in our models is that the active and passive stages of diapir growth are seldom or never reached, respectively. Only a few of the models show the characteristic upward flexure of bounding strata accompanying active rise on the field-scale (e.g. Fig. 3a, f) and plug like diapir stems with

vertical walls do not develop. Instead, most structures maintained their triangular shape throughout and appeared to grow more laterally than vertically. This behaviour could be due to continuous model sedimentation, preventing the overburden to become weak enough to completely thin. This interpretation is consistent with the models of Vendeville & Jackson (1992a) where an active and passive stage diapir stage were not observed when sedimentation accompanied overburden extension. It therefore seems possible that in basins with continuous sedimentation and extension many diapirs never evolve beyond the reactive stage, thus challenging the hypothesis of diapir evolution being dominated by passive growth. Alternatively, we note that many models showed repeated, short-lived periods of roof upward flexure and “flap rotation” (e.g. Fig. 2h) that would characterise active salt rise, but the recently exposed salt is rapidly buried beneath a new sedimentary cover (e.g. Fig. 3j). This forces the salt to revert to the reactive stage periodically and reflects a phased sediment deposition approach utilised in the models. This modelled behaviour might only be suitable for areas with temporally varying sedimentation rates, such as passive margins with periodic basin floor fan delivery. A further explanation for the failed materialisation of passive diapirism and long-term active salt rise might be the physical properties used for the sedimentary overburden. If the modelled overburden is too weak then salt piercement may not be maintained for long enough to enable long-term active and passive rise. Additionally, the remeshing algorithm used by Elfen might not have allowed for accurate “flap rotation” geometries to form, hence making it difficult to recognise active and passive growth.

The location of roof faults during diapir evolution considerably controls structural geometry. Should faults initiate proximal to the right-hand diapir flank, the opposite flank inherits a wide, low-angle section near the diapir crest (Fig. 2c), which provides an ideal focus area for sediment loading (Fig. 2j). This loading causes salt to migrate away from the flank and accentuating salt rise to a narrowing diapir apex (Fig. 2i-j). Where loading is significant, the diapir flanks are characterised by distinct high-angle and low-angle sections (e.g. Fig. 2m). Therefore, models where roof faults form off-centre develop an asymmetric diapir profile (e.g. Fig. 3g-h). This asymmetry exaggerates in models with fast extension (Fig. 3b) and sedimentation rates (Fig. 3g), initially short diapirs and thin pre-kinematic roof thickness (Fig. 3g compared to Fig. 3k and 3m respectively). Curved and triangular diapirs initiate with a narrow, central apex, constraining faults to this location and encouraging a symmetrical diapir to evolve. During geostatic initialisation of the models, establishment of a more pronounced loading gradient causes initially taller diapirs to arch their sedimentary cover upwards. Tall diapirs evolve symmetrically as faults tend to localize above the diapir crest where the salt is thick, and the roof is thin, and therefore, weak. Models where diapir flanks exhibit the above mentioned distinct high-angle and low-angle sections appear to develop broader, highly strained bounding overburden domains, reflecting complex salt-overburden interactions at these locations (e.g. Fig 3c, i, m).

The geometry of the adjacent syn-kinematic strata is highly variable between models and can be explained by the balance that exists between the extension rate, structure growth rate, and salt flow rate and availability in the case of a closed system (Fossen 2010), with direct implications for trap formation (Fig. 5). In models where salt supply outpaces generation of subsurface space e.g. lower extension rates, salt flow can sufficiently fill this space in addition to inflating the diapir and rotating syn-kinematic strata to steeper angles (Fig. 5a). Sediment loading can collapse the diapir flanks, causing the strata to fold and back-rotate to lower angles, creating a rim syncline sequence (Fig. 5b). Should subsurface space creation exceed salt supply e.g. thin salt layers, extensive collapse of the diapir flanks occurs which is also demonstrated in physical models by Vendeville & Jackson (1991). This creates distal, high-relief withdrawal structures (Fig. 5c). Analogue modelling by Vendeville & Jackson (1992b) indicated the diapir crest can collapse if flooded with sediment, which is supported by a developing depocenter above the diapir crest noted in model *D-TRI* (Fig. 3c). Each of these scenarios has a strong bearing on sediment-routing systems, and in turn, reservoir distributions, around salt diapirs (Fig. 5d); this knowledge is key for efficient field development planning.

Strain localisation along the diapir flanks as mentioned above was observed in all our models (Fig. 3), due to continuous subsidence of older, faulted strata. This indicates that the salt-sediment interface is a highly

deformed area where extensive small-scale faulting and fracturing can be expected. This has important implications for planning wells near salt structures and is supported by structural risk assessments carried out for a recently drilled exploration target in the Kwanza Basin offshore Angola (Fig. 6). Here, seismic data indicated the presence of small-scale faults above the diapir flanks (Fig. 6a) but these were considered as processing artefacts. However, the principal stress orientations predicted by our models and the associated orientation of shear fractures closely match those of the observed faults (Fig. 6b-d). Thus, strain localisation along diapir flanks provides a plausible explanation for the existence of these faults. Consequently, the mud weight design was optimised to minimise the risk for losses into a highly fractured section above the top salt and risk registers were updated to extend the risk of encountering fractured overburden down-flank from the diapir crest. An indicated alternative drilling location on Fig. 6a would avoid any seismically-resolvable faults. Nevertheless, as the flanks are thought to be a high strain environment, sub-seismic scale faulting may still pose a risk to drilling activities. This emphasises the value of geomechanical models for well placement and design even during early exploration stages. Furthermore, it fundamentally challenges the views of authors like Rowan *et al.* (2017) who believe that sediments bounding salt structures are rarely affected by faulting and fracturing and therefore do not constitute a risk to drilling activities.

Experiment 2: Reactivation of a basement step

In our second experiment we tested the impact of basement extension on salt structure development. The model was configured to have a pre-existing basement normal fault which was reactivated. Due to the pre-existing topography the overlying salt layer varied in thickness across the fault but had a flat top without initial pillows or diapirs.

The importance of basement architecture in controlling the evolution of salt structures in sedimentary basins has been inferred from many studies (e.g. Gaullier *et al.* 1993; Stewart & Coward 1995; Al Bahrani & McClay 2008; von Nicolai 2011; Dooley *et al.* 2017). The evolution of diapirs growing under thick-skinned tectonics follows similar principles to those of thin-skinned tectonics. When extensional stresses are applied the brittle sedimentary overburden thins and weakens via faulting and fracturing (Fig. 4a), whereas the viscous salt starts to flow into areas of reduced elevation and/or pressure heads (Fig. 4c). Salt rises reactively beneath grabens forming in the overburden and develops triangular salt pillows and rollers (Fig. 4e). With continued extension the reactive pillow may progress into a diapir and into active and passive stages as Dooley *et al.* (2003, 2005) demonstrated in their analogue experiments. Specific to thick-skinned tectonic settings, the evolving diapirs are situated above the basement footwall block near the fault scarp. Salt is fed from above the footwall and the hanging wall blocks until grounding of overburden strata onto the basement fault plane shuts off salt supply from the hanging wall block. From this point diapir growth is solely driven by salt movement above the footwall block.

There are two major differences between our models and those of Dooley *et al.* (2005). Firstly, our models suggest salt flow into the diapir occurs above the footwall block only, which is indicated by the direction of displacement vectors within the salt layer (Fig. 7). Flow from the hanging wall into the footwall is not observed, thus limiting the amount of salt available for pillow and diapir growth. This might account for the second apparent difference to the models of Dooley *et al.* (2005). As with the thin-skinned extension experiment the evolving structures remain in the reactive stage (e.g. Fig 4f) and do not grow into tall, narrow geometries that typify passive diapirs. Only when the overburden thickness was significantly reduced the early stages of active diapirism were reached (Fig. 4m). In all other models extension was predominantly accommodated by brittle faulting in the overburden and reactive salt rise into pillows and rollers. These results are consistent with the analogue models of Warsitzka *et al.* (2015). Their models, too, did not generate any high amplitude diapirs but produced rather subtle structures comparable to ours. They also demonstrate initial salt flow was only directed towards the downthrown basement block, similar to our models. Reverse salt flow towards the footwall was only enabled after extension had stopped, and continuous sedimentation in the rim

syncline had established a load gradient large enough for the salt to move in response to differential loading alone. Warsitzka *et al.* (2015) attributed the lack of an active and passive stage of diapirism in their models to the relatively short extension period, which was followed by a much longer phase of post-kinematic sedimentation. Contrary to this, extension in the models of Dooley *et al.* (2005) lasted throughout the duration of their experiment. Our results, where extension was also continuous but passive diapirism has not been achieved, do not support this hypothesis, and suggest that salt above the hanging wall block may have a limited role in feeding evolving footwall salt structures. This challenges the idea that overburden grounding onto the basement fault plane is a critical event for reducing salt availability for developing diapirs.

A simpler explanation for these described contrasting behaviours is the difference in model material properties used. To enhance diapirism Dooley *et al.* (2005) chose glass beads for their overburden material, which have a significantly reduced strength than the silica sands utilised by Warsitzka *et al.* (2015). Consequently, the overburden was breached more easily by the rising salt, promoting diapirism. In our models where the overburden has properties more similar to silica sands than glass beads, weakening of the sedimentary cover might also not have been extensive enough to allow for active and passive diapirism. This once more highlights the strong dependency of modelling results on the choice of input parameters.

Despite their pronounced differences all models show similar trends when the sensitivity tests are compared. Generally, a thick overburden (Fig. 4n) or high sedimentation rates (Fig. 4j) limits salt structure development due to the increased overburden strength. By contrast, a thicker salt layer promotes pillow/diapir growth since the frictional forces acting at the top and the base of the salt are relatively lower than with thin layers (Fig. 4l). A thick salt layer also promotes the decoupling of deformation below and above the salt, which manifests in different fault dips, larger offsets of subsalt and suprasalt faults and a wider deformation zone in the overburden (Fig. 4l). In all cases structures develop above the footwall basement block: this process is supported by seismic observations in many regions. For example, in the Central North Sea and Channel Basin deformation has localized in the footwall on rift margins overlying Zechstein salt, with corresponding diapiric activity (e.g. Stewart & Coward 1995; Stewart *et al.* 1996). For thin salt layers (Fig. 4k) the overburden and basement are closely coupled, and strain uptake may hard-link between the two, characterised by fault development above the basement fault (e.g. Stewart & Clark 1999).

This study also indicates that decoupling of deformation is enhanced by steeper basement faults (Fig. 4p) and lower slip rates (Fig. 4f). In the case of fast slip rates (Fig. 4h) multiple overburden structures develop and underlying salt pillows have a larger amplitude. This could be related to the more brittle response of the overburden when exposed to high strain rates and rapid flow of salt into the opening space beneath promoting diapir growth. We find that a thick overburden (Fig. 4n) and high sedimentation rates (Fig. 4j) also appears to enhance decoupling of deformation. Given that a thicker sedimentary cover is stronger, this increased offset is likely attributed to a larger flexural wavelength exhibited by strong overburden. This trend is also observed in early physical models (e.g. Vendeville *et al.* 1995; Ge & Vendeville 1997). In contrast to an early numerical experiment by Schultz-Ela & Jackson (1996), we do not observe development of overburden faults above the hanging wall basement block. This might be explained by lower extension rates used in our models, and we do see evidence of early stage strain localisation in our model *T-F2.5* run which utilises faster fault slip rates (Fig. 4h). We note that basement fault set-up has been improved in our study: a defined fault plane was explicitly modelled, and interpretation simplified by considering slip along one single fault rather than development of a basement graben.

The extent of overburden affected by basement faulting is particularly important in sedimentary basins where deep reservoirs are heavily cemented and natural fractures or hydraulic fracturing is required for commercial production of hydrocarbons. This is the case in Southern Oman, where recent exploration efforts have shifted towards early Proterozoic reservoirs whose structural history has strongly been controlled by movement of the underlying Cambrian Ara salt (Al-Barwani & McClay 2008) (Fig. 8). As part of the Arabian plate, which was

repeatedly affected by regional tectonic events, it is likely that basement faulting affected salt movement and hence the evolving deformation pattern in the reservoirs above. Figure 8a indicates a series of salt pillows and ridges which have developed parallel to basement extensional fault trends. These salt structures locate above basement fault footwall blocks as predicted by our models and are flanked by folded minibasin sequences (Fig. 8b). Salt structures appear to favour development above the large displacement and laterally continuous faults (Fig. 8a-b). Like our models, syn-kinematic sediments progressively infill topographic lows between structures (e.g. Fig. 4c vs. 4d), increasing the elastic thickness of the overburden and further reducing the likelihood of salt structures to develop above the footwall of neighbouring basement faults. Knowledge of the potential extent of a fault and fracture network within the sedimentary cover could be key to de-risk exploration targets and develop meaningful early commercial models. Given our predictions of strain localisation along the diapir flank due to successive burial of older, crestal faults, the presence of well-connected fracture networks, and thus, good reservoir deliverability might not be limited to diapir crests. Additionally, applying the model relationships discussed here to the distribution of suprasalt structures might provide clues on basement architecture in areas with poor sub-salt imaging.

Conclusions

Finite element modelling has successfully recreated field-scale salt structure evolution in two common tectonic settings: (a) evolution of a pre-existing diapir in response to thin-skinned extension, and (b) reactivation of a pre-existing basement fault beneath a salt layer (thick-skinned extension). The modelling results were compared to those of published analogue experiments, allowing us to examine concepts of diapir growth derived from these experiments. Additionally, we conducted model sensitivity analyses to examine the influence of different modelling parameters on salt structure evolution and the corresponding deformation pattern. We discuss the physical processes that account for variations in model evolution with comparison to previous analogue and numerical experiments and geological examples and discuss the merits of these new findings with application to hydrocarbon-related problems.

Modelled diapirs evolving in thin-skinned extensional settings closely resemble published analogue experiments. During reactive salt rise, active faulting is confined to the diapir crest and creates a triangular-shaped diapir. Older sequences are pushed aside and subside, thus highly strained domains bound the diapir flanks where extensive small-scale faulting and fracturing can be expected. Activity on these faults ceases during burial, however diapirs which exhibit distinct high-angle and low-angle sections on their flanks appear to develop broader strained domains. In some cases, these flank angle variations develop in model setups where the flank has a high tendency to collapse beneath a sediment load. This often occurs where roof faults initiate off-centre from the diapir crest, and thus providing an ideal focus area for sediment loading. Incremental loading and flank collapse create highly asymmetric diapir profiles observed in models with fast extension and sedimentation rates, initially short diapirs and thin pre-kinematic roof thicknesses. Curved and triangular diapirs focus faulting above a narrow crest, and thus develop a symmetrical profile. Salt supply to the diapir crestal area versus the distribution of sediment loading during diapir evolution has a pronounced impact on geometries in adjacent syn-kinematic strata, with implications for hydrocarbon trap development. Active and passive stages of diapir growth are seldom or never reached, respectively, suggesting that in basins with continuous sedimentation and extension many diapirs may never evolve beyond the reactive stage, thus challenging existing ideas that diapir evolution is dominated by passive growth.

In our thick-skinned extension experiment, entailing a reactivating basement fault beneath a salt layer, all models localise overburden faulting above the footwall basement block comparable to analogue and geological examples. Salt rises reactively beneath graben structures forming triangular salt pillows and rollers, which is inhibited by a thick overburden or high sedimentation rates but promoted by a thicker salt layer. In contrast to early analogue experiments, we do not see progression of salt pillows into diapirs with active and passive stages, and instead structures remain in the reactive stage as noted in more recent analogue

experiments. Only when overburden thickness, and thus strength, is significantly reduced do the early stages of active diapirism occur. Contrary to existing consensus, our models indicate that salt structures are fed salt above the footwall basement block only, thus the role of overburden grounding onto the basement fault scarp in limiting salt supply to evolving footwall structures is questioned. Decoupling of basement and overburden deformation is characterised by wider offsets of overburden faults from the basement fault scarp, wider deformation zones and different fault geometries. Deformation coupling increases with decreased salt thickness, overburden thickness, sedimentation rate, and fault angle, and increased fault slip rates.

An examination of discrepancies with other numerical and analogue experiments emphasises the importance of selecting appropriate modelling parameters when reconstructing salt tectonic settings. Although simple in setup, the described modelling technique may be extended to more detailed, prospect-specific models which might include further features not considered here. For example, coupled-seepage models could permit pore pressure prediction around evolving salt structures for informing drilling campaigns. Results presented in this study have shown application for resolving key drivers and sensitivities of salt flow and predicting distributions of overburden deformation, traps and sediment-routing systems. Hence this study highlights the increasing ability of numerical models to inform subsurface description in salt settings.

Acknowledgements

We would like to thank the support of the Subsurface Technical Centre at BP and Imperial College London, with special mentions to Jessica Miller, Rachael Arnold, Gary Hampson, Seb Turner, Lidia Lonergan and Joshua Griffiths. We also recognize contributions from Robin Eve and Dave Ashby, and technical support offered by Rockfield Global Ltd. We thank Ryan Thigpen and an anonymous reviewer for their comments.

References

- Al-Barwani, B. & McClay, K. 2008. Salt tectonics in the Thumrait area, in the southern part of the South Oman Salt Basin: Implications for mini-basin evolution. *GeoArabia*, **13**(4), 77-108.
- Albertz, M., Beaumont, C., Shimeld, J.W., Ings, S.J. & Gradmann, S. 2010. An investigation of salt tectonic structural styles in the Scotian Basin, offshore Atlantic Canada: 1. Comparison of observations with geometrically simple numerical models. *Tectonics*, **29**(4), <https://doi.org/10.1029/2009TC002539>
- Allen, P.A. & Allen, J.R. 2013. *Basin Analysis: Principles and Application to Petroleum Play Assessment*. Oxford, Wiley-Blackwell, pp. 632.
- Allen, J. & Beaumont, C. 2012. Impact of inconsistent density scaling on physical analogue models of continental margin scale salt tectonics. *Journal of Geophysical Research: Solid Earth*, **117**(B8), <https://doi.org/10.1029/2012JB009227>
- Archer, S.G., Alsop, G.I., Hartley, A.J., Grant, N.T. & Hodgkinson, R. 2012. Salt tectonics, sediments and prospectivity: an introduction. In: Alsop, G.I., Archer, S.G., Hartley, A.J., Grant, N.T. & Hodgkinson, R. (eds) *Salt Tectonics, Sediments and Prospectivity*. Geological Society, London, Special Publications, **363**, p. 1-6.
- Crook, A.J.L., Owen, D.R.J., Willson, S.M. & Yu, J.G. 2006. Benchmarks for the evolution of shear localisation with large relative sliding in frictional materials. *Computer Methods in Applied Mechanics and Engineering*, **195**(37-40), 4991-5010.
- Dooley, T., McClay, K.R., & Pascoe, R. 2003. 3D analogue models of variable displacement extensional faults: applications to the Revfallet Fault system, offshore mid-Norway. *Geological Society, London, Special Publications*, **212**, 151-167.
- Dooley, T., McClay, K.R., Hempton, M. & Smit, D. 2005. Salt tectonics above complex basement extensional fault systems: results from analogue modelling. In: Doré, A.G. & Vining, B.A. (eds) *Petroleum Geology: North-West Europe and Global Perspectives*. Proceedings of the 6th Petroleum Geology Conference, 1631-1648.
- Dooley, T.P., Hudec, M.R., Carruthers, D., Jackson, M.P.A & Luo, G. 2017. The effects of base-scale relief on salt flow and suprasalt deformation patterns – Part 1: Flow across simple steps in the base of salt. *Interpretation*, **5**(1), 1-23.
- Fossen, H. (eds) 2010. *Structural Geology*. Cambridge, Cambridge University, pp. 480.

- Gaullier, V., Brun, J.P., Gue, G. & Lecanu, H. 1993. Raft tectonics: the effects of residual topography below a salt de' collement. *Tectonophysics*, **228(3-4)**, 363-381.
- Ge, H. & Vendeville, B.C. 1997. Influence of active subsalt normal faults on the growth and location of suprasalt structures. *Gulf Coast Association of Geological Societies Transactions*, **47**, 169-176.
- Ge, H., Jackson, M.P.A. & Vendeville, B.C. 1997. Kinematics and Dynamics of Salt Tectonics Driven by Progradation. *AAPG Bulletin*, **81(3)**, 398-423.
- Gemmer, L., Beaumont, C. & Ings, S.J. 2005. Dynamic modelling of passive margin salt tectonics: effects of water loading, sediment properties and sedimentation patterns. *Basin Research*, **17(3)**, 383-402, <https://doi.org/10.1111-j.1365-2117.2005.00274.x>
- Gemmer, L., Ings, S.J., Medvedev, S. & Beaumont, C. 2004. Salt tectonics driven by differential sediment loading: Stability analysis and finite element experiments. *Basin Research*, **16(2)**, 199-218.
- Gradmann, S., Beaumont, C. & Albertz, M. 2009. Factors controlling the evolution of the Perdido Fold Belt, northwestern Gulf of Mexico, determined from numerical models. *Tectonics*, **28(2)**, <https://doi.org/10.1029/2008TC002326>
- Hodgson, N.A., Farnsworth, J. & Fraser, A.J. 1992. Salt-related tectonics, sedimentation and hydrocarbon plays in the Central Graben, North Sea, UKCS. In: Hardman, R.F.P. (eds) *Exploration Britain: Geological insights for the next decade*. Geological Society Special Publication, **67**, 31-63.
- Hudec, M.R. & Jackson, M.P.A. 2007. Terra infirma: Understanding salt tectonics. *Earth-Science Reviews*, **82**, 1-28.
- Krantz, R.W. 1989. Fault inversion in scaled experimental models. *Bulletin of Geological Society of America*, **21**, 176.
- Kukal, Z. 1990. The rate of geological processes. *Earth-Science Reviews*, **28**, 1-284.
- Luo, G., Nikolinakou, M., Flemings, P.B. & Hudec, M.R. 2012. Geomechanical modelling of stresses adjacent to salt bodies: Part 1 – Uncoupled models. *AAPG Bulletin*, **96(1)**, 43-64.
- Nelson, R.A. 2001. *Geologic Analysis of Naturally Fractured Reservoirs*. Boston, Gulf Professional Publishing, pp. 332.
- Pizarro, J.O.D.S & Branco, C.C.M. 2012. Challenges in implementing an EOR project in the pre-salt province in Deep Offshore Brasil. In: *SPE EOR Conference at Oil and Gas West Asia, Society of Petroleum Engineers, 2012*.
- Reddy, J.N. 1993. *An introduction to the finite element method*. New York, McGraw-Hill.
- Rockfield Global 2010. *ELFEN Forward Modeling User Manual*. Rockfield Software Limited.
- Rockfield Global 2015. *ELFEN Explicit Manual*. Rockfield Software Limited.
- Rowan, M.G., Munoz, J.A., Roca, E., Fischer, M. & Giles, K.A. 2017. Rock Deformation Adjacent to Salt Diapirs. *AAPG/SEG International Conference and Exhibition*, London, England.
- Rowan, M.G., Peel, F.J. & Vendeville, B.C. 2004. Gravity-driven fold belts on passive margins. In: McClay, K.R. (eds) *Thrust Tectonics and hydrocarbon systems*. **AAPG Memoir 82**, 157-182.
- Schultz-Ela, D.D. & Jackson, M.P.A. 1996. Relation of Subsalt Structures to Suprasalt Structures During Extension. *AAPG Bulletin*, v. **80(12)**, 1896-1924.
- Seni, S.J. & Jackson, M.P.A. 1983. Evolution of salt structures, east Texas diapir province, part 1: Sedimentary record of halokinesis. *AAPG Bulletin*, **67(8)**, 1219-1244.
- Stewart, S.A. & Clark, J.A. 1999. Impact of salt on the structure of the Central North Sea hydrocarbon fairways. In: Fleet, A.J. & Boldy, S.A.R. (eds) *Petroleum Geology of Northwest Europe: Proceedings of the 5th Conference*, 179-200.
- Stewart, S.A. & Coward, M.P. 1995. Synthesis of salt tectonics in the southern North Sea, UK, *Marine and Petroleum Geology*, **12(5)**, 457-475.
- Stewart, S.A., Harvey, M.J., Otto, S.C. & Weston, P.J. 1996. Influence of salt on fault geometry: examples from the UK salt basins. In: Alsop, G.I., Blundell, D.J. & Davison, I. (eds) *Salt Tectonics*, Geological Society Special Publication, **100**, 175-202.
- Talbot, C.J., Megvedev, S., Alavi, M., Shahrivar, H. & Heidari, E. 2000. Salt extrusion at Kuh-e-Jahani, Iran, from June 1994 to November 1997. Geological Society, London, Special Publications, **174**, 93-110, <https://doi.org/10.1144/GSL.SP.1999.174.01.06>.
- Thigpen, J.R., Roberts, D., Snow, J.K., Walker, C.D. & Bere, A. 2019. Integrating kinematic restoration and forward finite element simulations to constrain the evolution of salt diapirism and overburden deformation in evaporite basins. *Journal of Structural Geology*, **118**, 68-86.
- Thornton, D.A. & Crook, A.J.L. 2014. Predictive Modeling of the Evolution of Fault Structure: 3-D Modeling and Coupled Geomechanical/Flow Simulation. *Rock Mechanics and Rock Engineering*, **47(5)**, 1533-1549.
- Trusheim, F. 1960. Mechanism of salt migration in northern Germany. *AAPG Bulletin*, **44(9)**, 1519-1540.

- Vendeville, B.C. & Jackson, M.P.A. 1991. Deposition, extension, and the shape of downbuilding salt diapirs. *AAPG Bulletin*, **75**(3).
- Vendeville, B.C. & Jackson, M.P.A. 1992a. The rise of diapirs during thin-skinned extension. *Marine and Petroleum Geology*, **9**(4), 331-354.
- Vendeville, B.C. & Jackson, M.P.A. 1992b. The fall of diapirs during thin-skinned extension. *Marine and Petroleum Geology*, **9**(4), 354-371.
- Vendeville, B.C., Ge, H. & Jackson, M.P.A. 1995. Scale models of salt tectonics during basement-involved extension. *Petroleum Geoscience*, **1**(2), 179-183.
- von Nicolai, C. 2011. The interplay of salt movements and regional tectonics at the passive continental margin of the South Atlantic, Kwanza Basin. PhD thesis, Universität Potsdam.
- Warsitzka, M., Kley J. & Kukowski, N. 2013. Salt diapirism driven by differential loading—Some insights from analogue modelling. *Tectonophysics*, **591**, 83-97.
- Warsitzka, M., Kley, J. & Kukowski, N. 2015. Analogue experiments of salt flow and pillow growth due basement faulting and differential loading. *Solid Earth Discussion*, **6**(1), 9-31.

Figure captions

Fig. 1. Numerical experiment designs for (a-b) Experiment 1: Diapir evolution under extension, and (c) Experiment 2: Reactivation of a basement step. Default model geological parameters are indicated, which are altered for conducting sensitivity analysis. Average model horizontal strain rates are (a) $1.98 \times 10^{-15} \text{ s}^{-1}$, and (c) $6.6 \times 10^{-16} \text{ s}^{-1}$, respectively.

Fig. 2. (a-j) Experiment 1: Diapir evolution under extension, reference model run (*D-REF*). Parts (a), (c), (e), (g), (i) and (j) describe model evolution. Parts (b), (d), (f) and (h) are detailed close-ups as indicated. Figures are contoured by effective plastic strain.

Fig. 3. Experiment 1 sensitivity analysis, detailing the influence of geological parameters on diapir salt movement and structural development. Altered geological parameters include (a-b) extension rate, (c-d) diapir shape, (e-g) sedimentation rate, (h-i) salt layer thickness, (j-k) diapir height, and (l-m) roof thickness. Figures are contoured by effective plastic strain or accumulated vertical displacement (y-axis), as indicated.

Fig. 4. Experiment 2: Reactivation of a basement step. (a-f) Reference model run (*T-REF*) evolution. (g-p) Sensitivity analysis, detailing the influence of geological parameters on salt movement and structural development. Altered geological parameters include (g-h) fault slip rate, (i-j) sedimentation rate, (k-l) salt layer thickness, (m-n) overburden thickness, and (o-p) basement fault angle. Figures are contoured by effective plastic strain or effective plastic strain rate, as indicated.

Fig. 5. Influence of diapir evolution on prospectivity. (a) Progressive diapir inflation creates high-angle salt flank and subtle 4-way traps proximal to the diapir. (b) Diapir inflation followed by flank deflation develops a mixture of trap styles. (c) Extensive diapir flank deflation creates turtle-style 4-way traps, assuming other diapirs have developed out of section. (d) Schematic of sediment dispersal patterns and reservoir distributions for a time-slice in (a). The rim syncline sequence continues to fold as salt rises; therefore, the apparent syncline axis may not reflect the sediment fairway axis in older units.

Fig. 6. Case Study: Kwanza Basin, offshore Angola. (a) An interpreted seismic section through a salt diapir, perpendicular to the regional structural orientation. Small-scale faults were identified above the diapir flank near the location of a proposed well, however these were disregarded as processing artefacts (b) Model *D-ROLL*, developed from an initial long-wavelength salt pillow (8.0 Ma), compares well to the interpreted salt diapir. Yielding in Shear Flag contours suggests fracture development above the crest of the salt wall, and within strained stratal tips above the diapir flanks. (c-d) Stress tensor analysis predicts the development of extensional shear fractures with similar orientations to faults observed in the seismic section. Strain can localise along the flank during diapir evolution; therefore, these faults are unlikely to be seismic artefacts and may pose drilling risks for the proposed well.

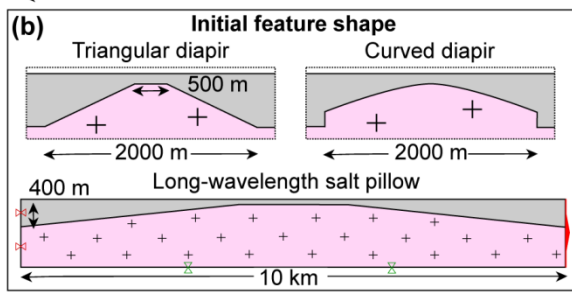
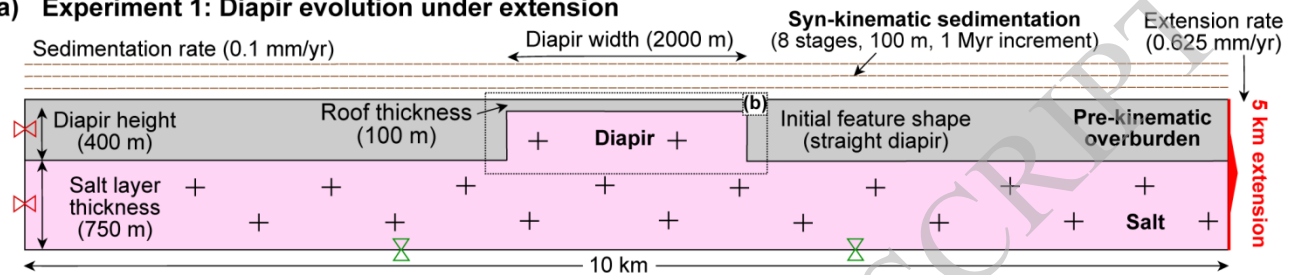
Fig. 7. Experiment 2 reference model (*T-REF*, 900 kyr). Salt layer velocity vectors indicate complex flow patterns in response to loading. Salt is drawn into the low-pressure zone beneath the hourglass structure, indicated by helical flow, and is expelled over the basement step during overburden grounding.

Fig. 8. Case Study: South Oman Salt Basin. (a) Two-way travel time map for the Top Ara Salt in the Thumrait area, South Oman Salt Basin, overlain with basement fault polygons (location indicated on the Oman regional inset map). Lower values (red) indicate salt walls and ridges, and higher values (blue) indicate minibasins. (b) Interpreted seismic section through salt ridges in the Thumrait area (location indicated in (a)). Basement fault orientations align to minibasin and salt structure trends; however, in many cases are significantly offset into the footwall cover of the basement fault. Salt ridges often locate above the footwall of the largest displacement

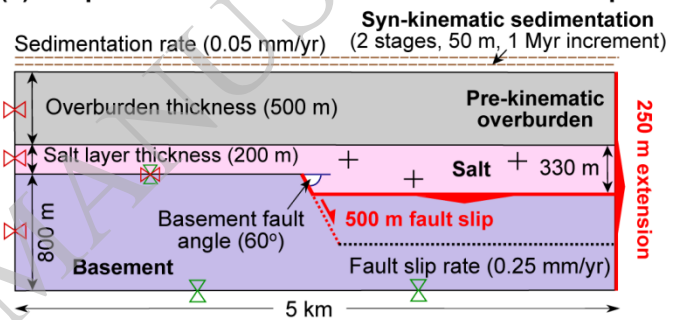
fault, whilst salt evacuates above smaller displacement faults, developing a thick syn-kinematic overburden cover sequence. Figures modified from Al-Barwani & McClay (2008).

ACCEPTED MANUSCRIPT

(a) Experiment 1: Diapir evolution under extension



(c) Experiment 2: Reactivation of a basement step



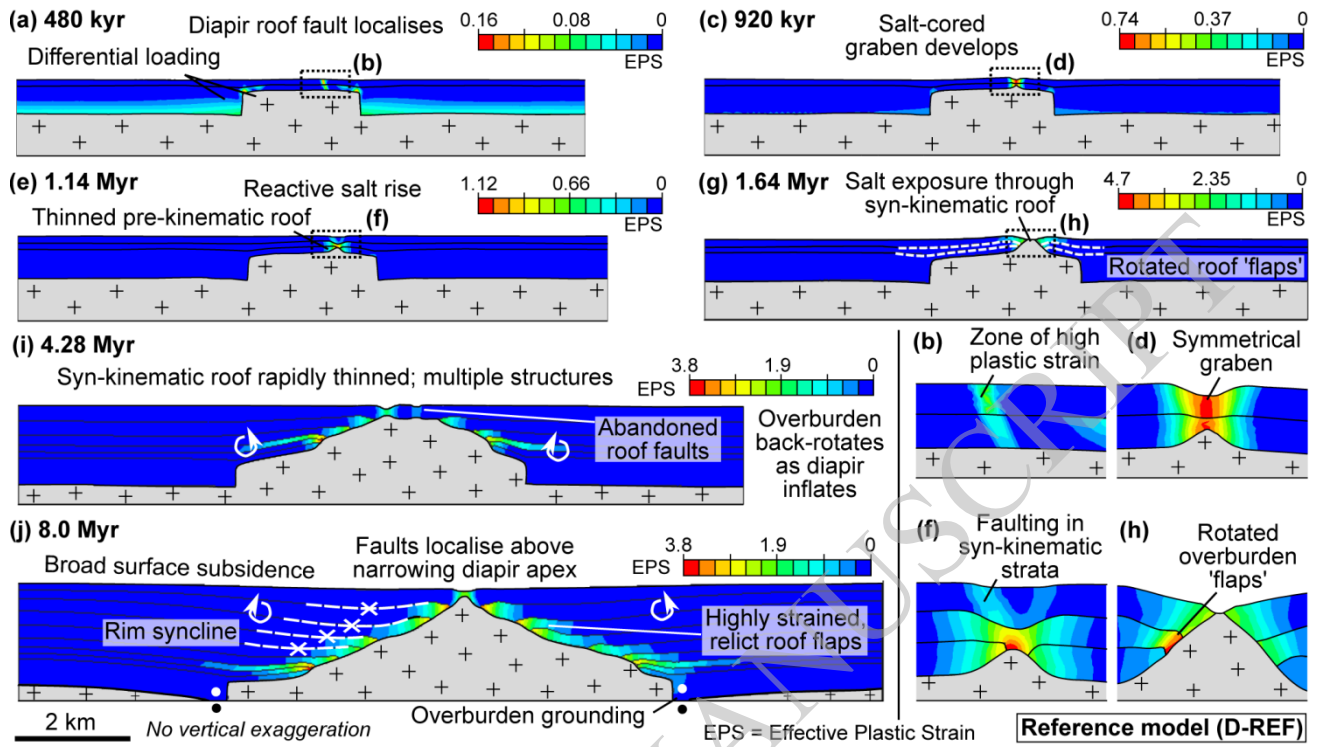
Y
X

Tectonic loading (direction arrow)

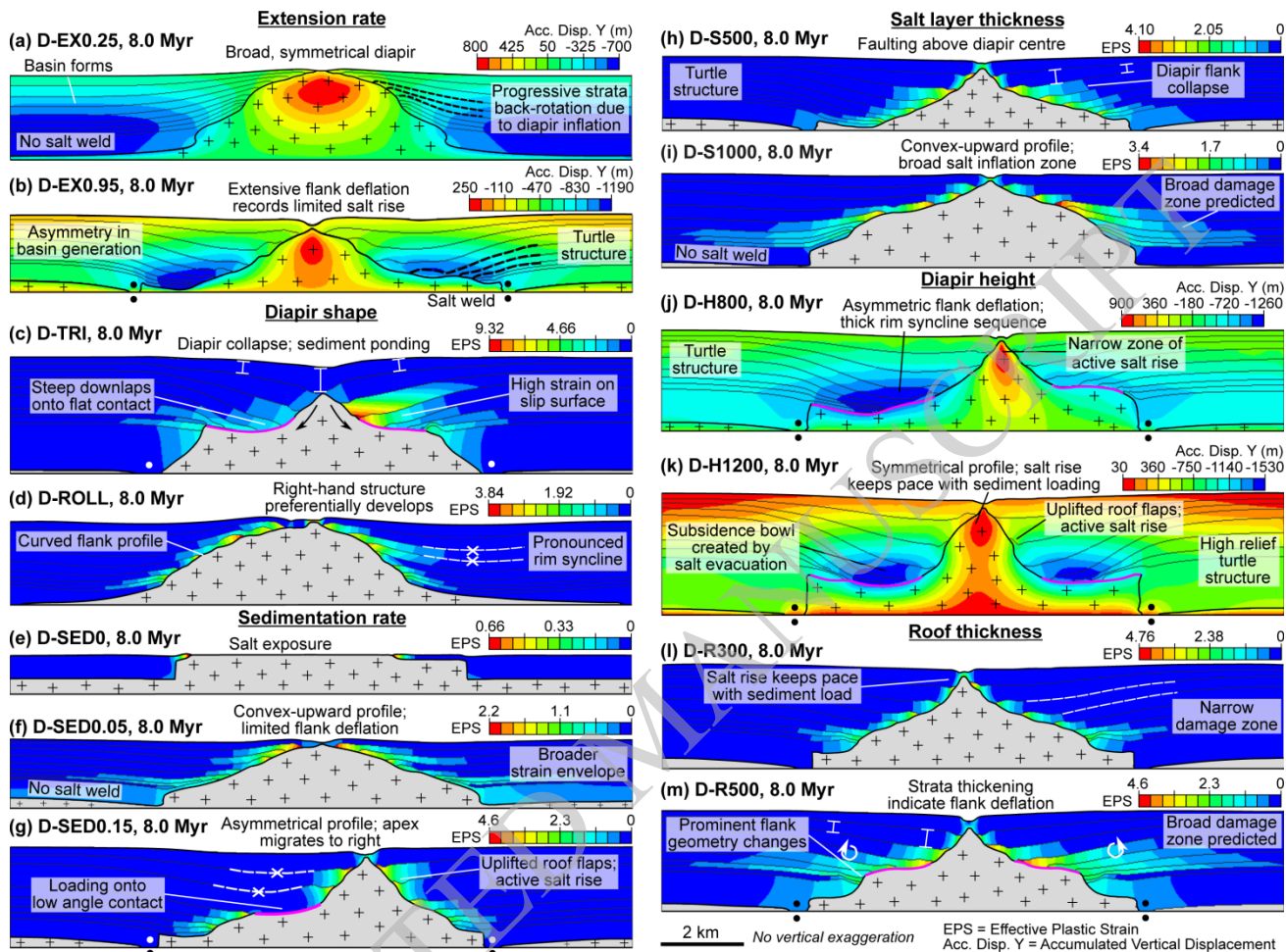
Fixed vertically

Fixed horizontally

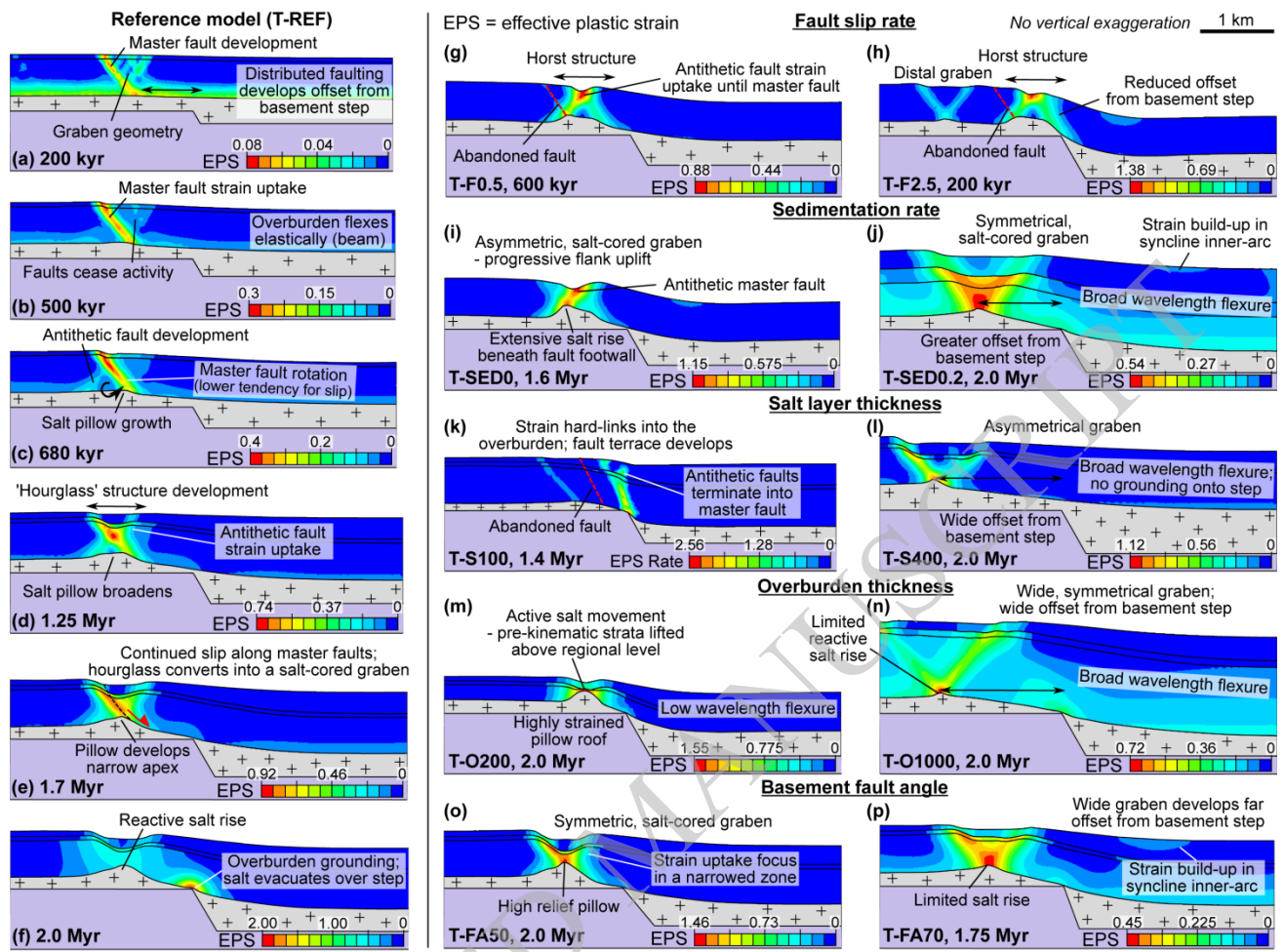
ACCEPTED



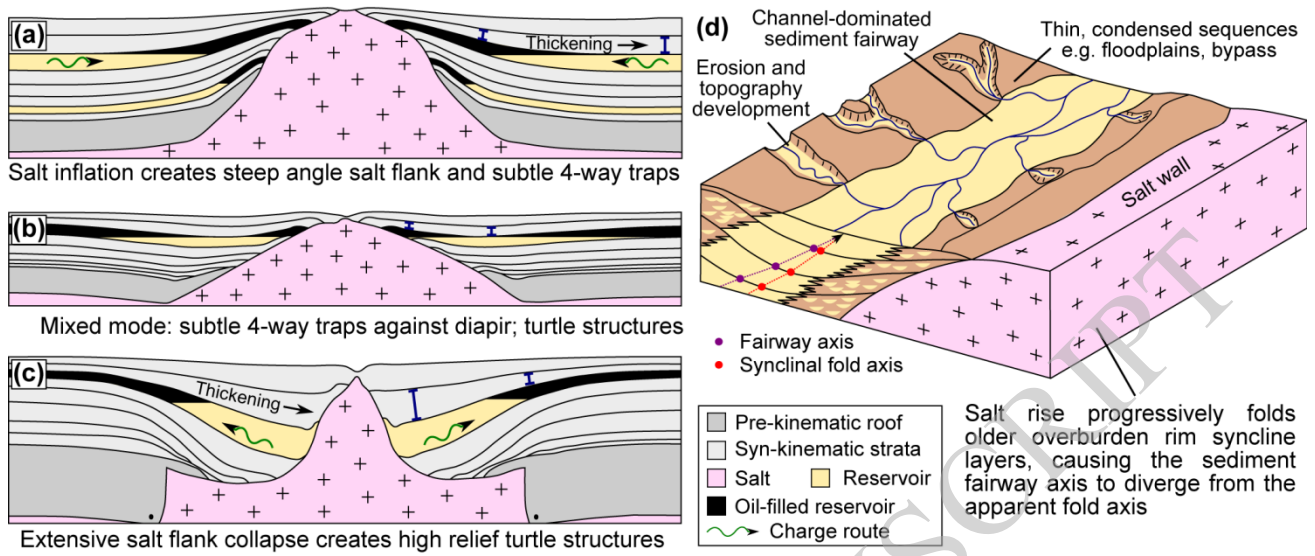
ACCEPTED MANUSCRIPT



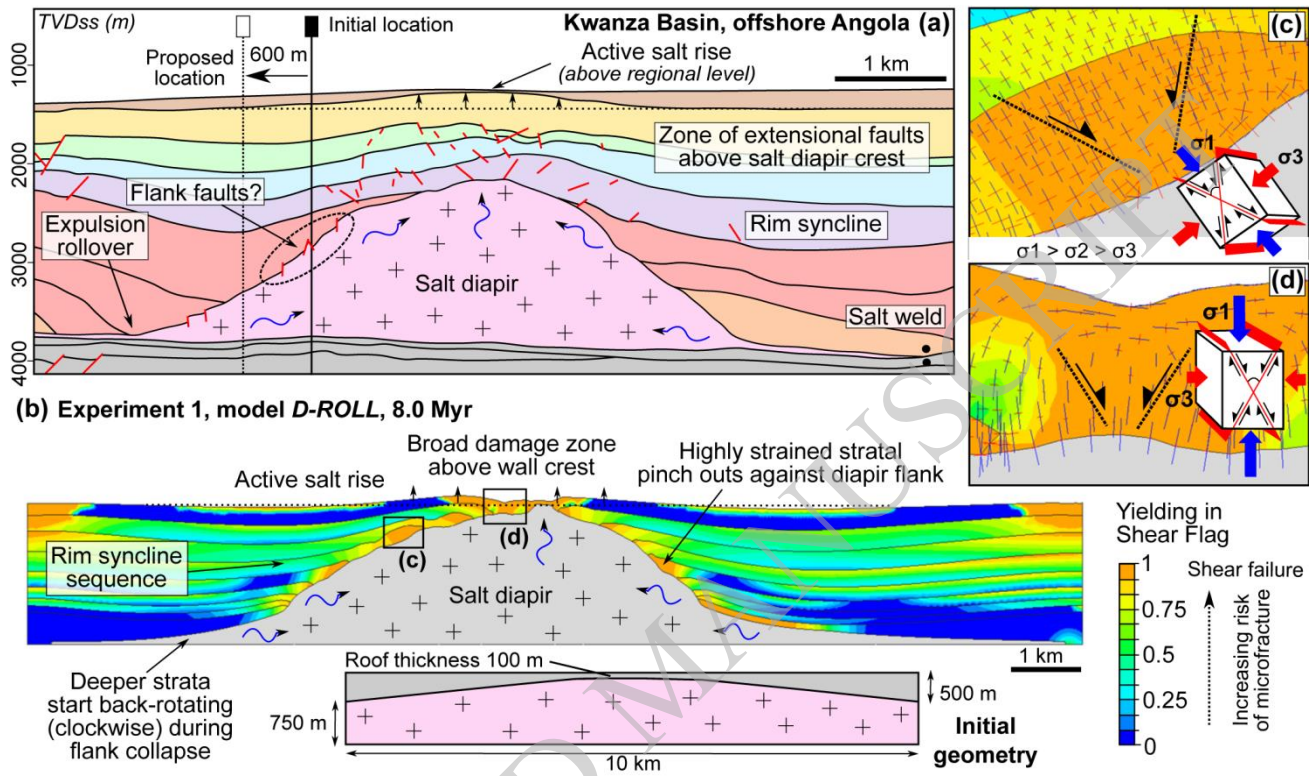
ACCEPTED



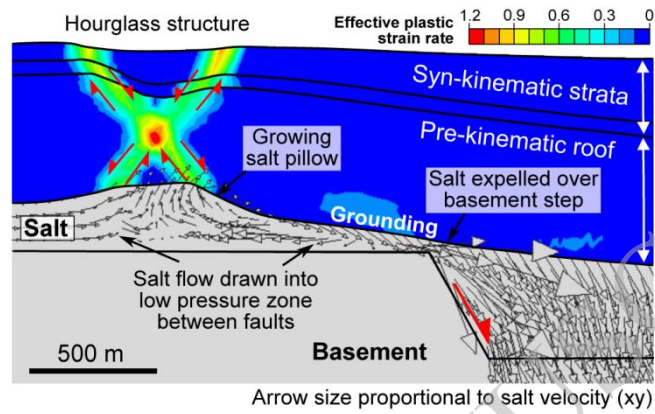
ACCEPTED



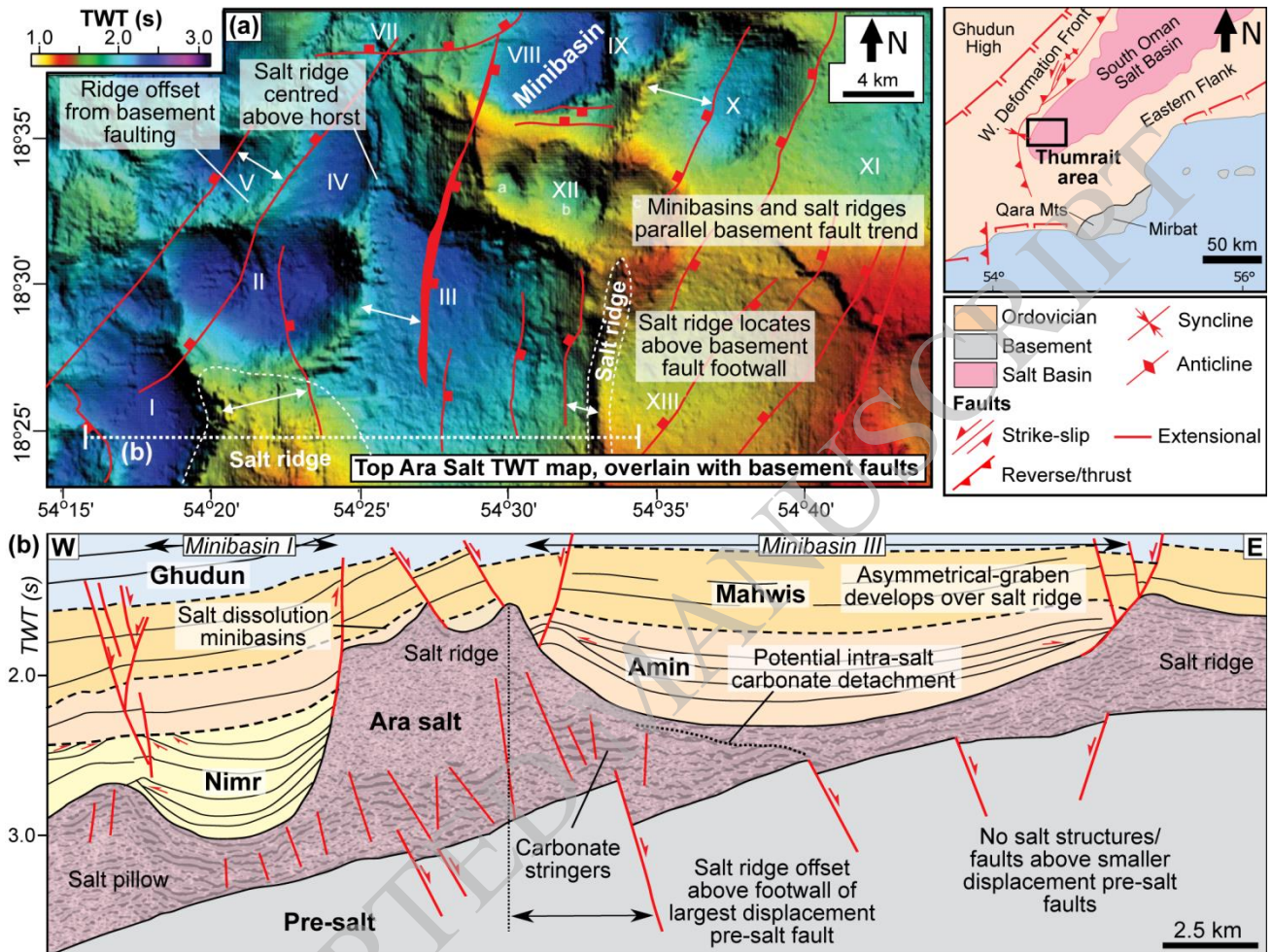
ACCEPTED MANUSCRIPT



ACCEPTED



ACCEPTED MANUSCRIPT



Tables

Table 1. Description of tested geological parameters. *D-REF* and *T-REF* are reference models for the two experiments, which utilise default parameter values as specified. Additional models (in bold) utilise default parameters as with the reference case, but vary one parameter as specified for sensitivity analysis

<i>Experiment 1 – Diapir evolution under extension</i>							
Parameter	D-REF	Sensitivity analysis					
Extension rate (mm/yr)	0.625	D-EX0.25	0.25	D-EX0.95	0.95		
Initial feature shape	Straight diapir	D-CURV	Curved diapir	D-TRI	Triangular diapir	D-ROLL	Salt pillow
Sedimentation rate (mm/yr)	0.1	D-SED0	0	D-SED0.05	0.05	D-SED0.15	0.15
Salt layer thickness (m)	750	D-S500	500	D-S1000	1000		
Diapir width (m)	2000	D-W1000	1000	D-W3000	3000		
Diapir height (m)	400	D-H800	800	D-H1200	1200		
Roof thickness (m)	100	D-R300	300	D-R500	500		
<i>Experiment 2 – Reactivation of a basement step</i>							
Parameter	T-REF	Sensitivity analysis					
Fault slip rate (mm/yr)	0.25	T-F0.5	0.5	T-F1.0	1.0	T-F2.5	2.5
Sedimentation rate (mm/yr)	0.05	T-SED0	0	T-SED0.2	0.2		
Salt layer thickness (m)	200	T-S100	100	T-S400	400		
Overburden thickness (m)	500	T-O200	200	T-O1000	1000		
Basement fault angle (°)	60	T-FA50	50	T-FA70	70		

Table 2. Mechanical properties for finite element model materials

<i>Overburden & syn-kinematic sedimentation</i>	
Young's modulus (E)	200 MPa
Poisson's ratio (ν)	0.2
Bulk density (ρ_b)	2400 kg m ⁻³
Initial porosity	0.40
Pore fluid density (ρ_f)	1000 kg m ⁻³
<i>Basement</i>	
Young's modulus (E)	20000 MPa
Poisson's ratio (ν)	0.25
Density (ρ)	2400 kg m ⁻³
<i>Salt</i>	
Young's modulus (E)	1000 MPa
Poisson's ratio (ν)	0.35
Density (ρ)	2200 kg m ⁻³
Viscosity (μ)	0.3 Pa Ma

Table 3. Reconciliation of geological parameter values utilised in finite element models within this study.

Parameter	Range tested	Justifications
Extension rate / fault slip rate	0.1-2.5 mm/yr	Strain rates on many rifts and passive margins typically lie between 10^{-14} s^{-1} to 10^{-16} s^{-1} (Allen and Allen 2013), equivalent to average extension rates between 0.03 to 3 mm/yr on a field-scale (10 km). Tested ranges also lie within estimated ranges for rifting (0.1-10 mm/yr) and continental margin subsidence (0.02-0.5 mm/yr) by Kukal (1990).
Initial feature shape	Straight, triangular, curved diapirs; salt pillow	A range of diapir geometries are observed in nature, for example reactive diapirs are often triangular in profile, and passive diapirs tend to have straight sides. Curved geometries are likely to form under high sedimentation rates (Hudec & Jackson 2007).
Sedimentation rate	0-0.3 mm/yr	Allen & Allen (2013) indicate a wide range of sedimentation rates (0.1-10 mm/yr) are possible, encompassing different depositional environments. The fastest rates are not considered to limit model scale.
Salt layer thickness	100-1000 m	Salt layers can reach 2 km thick in the Santos-Campos Basin (Pizarro & Branco 2012). It is thought that salt layers below 100 m are insufficient for significant salt flow, due to shearing against country rock (e.g. Nelson 2001; Hudec & Jackson, 2007).
Diapir width	1000-3000 m	A range of diapir widths are observed in nature, and we consider a range of field-scale widths.
Diapir height	400-1200 m	A wide range of diapir heights are observed in nature. An upper limit has been ascribed to limit model scale.
Overburden thickness	100-1000 m	A range of overburden thicknesses are considered, representing sediment-rich and sediment-poor systems. The upper limit is ascribed to restrict model scale; in addition, very thick pre-kinematic roofs may be inappropriate as halokinesis is thought to occur quickly in response to sediment deposition (Seni & Jackson 1983)
Basement fault angle	50-70°	Extensional faults initiate with dips around 60°, however basement blocks can subsequently rotate to steeper or shallower angles (e.g. Fossen 2010).